International Journal of Fatigue 138 (2020) 105696

Contents lists available at ScienceDirect

International Journal of Fatigue

journal homepage: www.elsevier.com/locate/ijfatigue

Very-high-cycle fatigue behavior of AlSi10Mg manufactured by selective laser melting: Effect of build orientation and mean stress

Guian Qian[a,b], Zhimo Jian[a,b], Yujia Qian[c], Xiangnan Pan[a,b], Xianfeng Ma[c,*], Youshi Hong[a,b,*]

[a] State Key Laboratory of Nonlinear Mechanics (LNM), Institute of Mechanics, Chinese Academy of Sciences, Beijing 100190, China
[b] School of Engineering Science, University of Chinese Academy of Sciences, Beijing 100049, China
[c] Sino-French Institute of Nuclear Engineering and Technology, Sun Yat-Sen University, Zhuhai 519082, Guangdong, China

ARTICLE INFO

Keywords:
Selective laser melting
Very-high-cycle fatigue
AlSi10Mg
Crack initiation
Fatigue strength

ABSTRACT

This paper studies the influence of build orientation and mean stress on the very-high-cycle fatigue (VHCF) behavior of AlSi10Mg fabricated by selective laser melting (SLM). Horizontally built specimens demonstrate better mechanical performance than vertically built specimens. Four crack initiation modes are identified for the specimens in high-cycle fatigue (HCF) and VHCF regimes, namely initiation by lack-of-fusion, initiation by internal pore, initiation with no obvious defect and initiation by tearing. Moreover, it turns out that the mean stress accelerates crack initiation, and hence reduces fatigue life. A model is proposed to describe the effect of crack initiation location on fatigue strength.

1. Introduction

Additive manufacturing (AM) technology is a new frontier technology that directly processes parts by layers according to three-dimensional digital model [1]. Among all AM technologies, selective laser melting (SLM) has attracted considerable academic attention [2,3], which is a process of melting and cooling metal powder rapidly by a high energy laser. This process is based on the interaction between laser and powder which includes a series of physical and chemical processes such as energy transfer and state change. SLM has been widely employed for AM of metals and alloys, such as Ti6Al4V, AlSi10Mg and Inconel 718 [4]. The SLM process provides an alternative to manufacture components with unique microstructures [5-7]. Despite many research efforts on the optimization of SLM process parameters, a defect-free component with uniform microstructures has not been fully achieved [8]. For example, the complex interactions between laser and powder can lead to the formation of pores in SLM materials [9,10]. The influence of SLM processing parameters on fabricated components has been extensively investigated. It is found that the laser power could affect the porosity of SLM materials [11]. The power of laser must be selected carefully because neither too high nor too low power leads to low porosity. In order to fully industrialize this technology for load bearing components, it is critical to characterize and understand the effect of microstructures properly on mechanical properties of materials manufactured by SLM, especially under cyclic loadings [10,12-14].

Recently, studies found that the static mechanical properties of SLM alloys are much better than those by traditional casting [15]. However, in real engineering application there is a high chance of having geometrical discontinuities in the AM parts, which can consequently influence the stress concentration and the fatigue behavior of the part [16-19]. Therefore, the fatigue properties of SLM alloys need to be fully understood [16-18]. A lot of methods can be used to study the fatigue mechanism and the corresponding fatigue lifetime [19-31]. Among different factors, build orientation is an important parameter and has been investigated frequently. Some results [32,33] showed no obvious influence of build orientation on fatigue performance, whereas it is reported [15] that there is about 25% difference in fatigue strength between horizontally and vertically built parts. A thorough understanding is needed for the relationships among process parameters, microstructure and mechanical properties.

For the fatigue analysis of AlSi10Mg made by SLM, it is general accepted that heat treatment will improve the fatigue performance as it reduces internal pores [34,35]. Surface polishing improves fatigue performance [36], whereas tensile mean stress reduces the fatigue life of SLM materials [37]. However, the very-high-cycle fatigue (VHCF) properties of SLM AlSi10Mg need to be fully understood.

This paper aims to understand the influence of build orientation and mean stress on high-cycle fatigue (HCF) and VHCF properties of SLM fabricated AlSi10Mg. Special attention is paid to the crack initiation mechanism in the specimens with different build orientations. A model

* Corresponding authors.
E-mail addresses: maxf6@mail.sysu.edu.cn (X. Ma), hongys@imech.ac.cn (Y. Hong).

https://doi.org/10.1016/j.ijfatigue.2020.105696
Received 29 December 2019; Received in revised form 3 May 2020; Accepted 4 May 2020
Available online 14 May 2020

Table 1
Nominal chemical composition of AlSi10Mg specimen (wt. %).

Element	Al	Si	Mg	Fe	Ti	Cr	Cu	Mn	Ni	V	Zn
wt. %	Balance	9.75	0.22	0.092	0.011	< 0.01	< 0.01	< 0.01	< 0.01	< 0.01	< 0.01

is proposed to describe the effect of crack initiation location on fatigue strength.

2. Material, specimens and experimental procedure

2.1. Material

The nominal chemical composition of the AlSi10Mg specimens for tensile and fatigue tests manufactured by SLM process is listed in Table 1 [38].

2.2. Specimen

In order to investigate the influence of building orientation, specimens with two orientations, namely vertically (90°) built and horizontally (0°) built, were used in tensile and fatigue test experiments. The tensile tests were conducted on standard dog bone specimens (Fig. 1a and b) to obtain basic mechanical properties of this material. Fig. 1a shows the geometry of the specimen and Fig. 1c shows the side views of fracture specimens with two build orientations (0° and 90°). The average surface roughness of the AlSi10Mg specimens is 2.526 μm. In the tensile experiment, four specimens in each printing direction were tested.

In fatigue tests, hourglass shape specimens (Fig. 2a and b) with two build orientations were used. The build orientation is the layer added direction, as shown in Fig. 2c.

2.3. Selective laser melting process

Fig. 3 shows the schematic of selective laser melting process, in which a fiber laser is adopted and the laser beam irradiates the base to melt the metal powder through the scanning mirror. Then the metal powder melts and solidifies rapidly to form one layer of the component, and the base will drop one layer after scanning and the powder pool will feed the powder. Thus the required components will be formed. The related SLM processing parameters used in this paper are listed in Table 2.

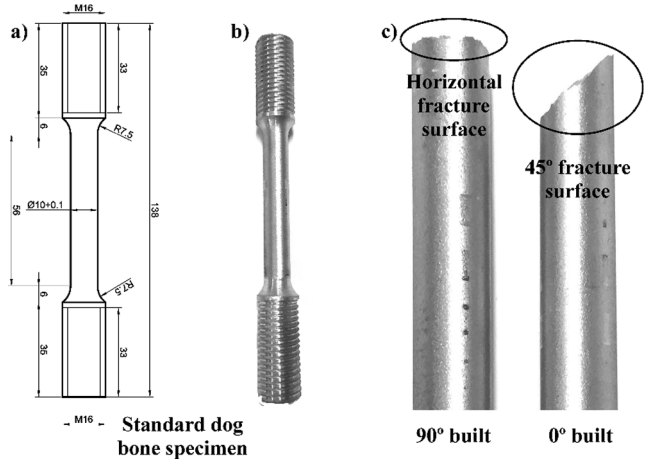

Fig. 1. Standard dog bone specimen for tensile test: a) geometry of specimen (dimensions in mm), b) specimen photo and c) side views of fracture specimens with two build orientations.

2.4. Tensile tests

The design of the tensile test specimens of AlSi10Mg is according to the Chinese standard of GB/T228-2002. For each group of specimens printed with different orientations, standard dog bone specimens were tested at a loading rate of 2 mm/min.

2.5. Ultrasonic fatigue tests

The test equipment for fatigue experiment is an ultrasonic fatigue testing machine (Lasur GF20-TC) equipped with a tensile machine, as shown in Fig. 4. It also consists of a ventilation system, which was designed to eliminate the potential temperature increase of specimen due to ultrahigh frequency vibration. The experimental principle of ultrasonic fatigue machine is the resonance of the specimen. A resonance frequency of 20 kHz was used for the tests. Therefore, the experiments were carried out under displacement control in the range from 2.2 μm to 21.5 μm according to the stress–strain relationship (the stress range is from 40 MPa to 390 MPa). The temperature was kept at room temperature during the experiment. An advantage of this equipment is that fatigue experiment could be performed with tensile mean stress. As a result, it is possible to investigate the effect of tensile mean stress on fatigue life of specimen.

3. Results and discussion

3.1. Stress–strain curve

Fig. 5 presents the engineering stress versus engineering strain for the specimens with two build orientations. It is clear that 0° built specimen has better mechanical properties than 90° built specimen, especially in terms of ultimate elongation. The values of yield strength (YS) of 0° and 90° built specimens are 270 MPa and 235 MPa, respectively. The ultimate tensile stress (UTS) of 0° built specimen is 465 MPa and that for 90° built specimen is 440 MPa, which is in line with [39]. The elongation of 0° built (12.7%) specimen is far better than that of 90° built (4.3%), similar to the result in [40]. For the 0° built specimen, the loading direction is perpendicular to layer added direction while for 90° built specimen, the loading direction is parallel with layer added direction. The side view of fracture surface in Fig. 1c shows clearly the difference. The 90° built specimen has horizontal fracture surface while the 0° built specimen has 45° fracture surface. Shear stress plays a more important role in the fracture of 0° built specimen while tensile stress is the key stress in the fracture of 90° built specimen.

3.2. Microstructures

It is well known that materials fabricated by SLM demonstrate anisotropy and heterogeneity characteristics [41,42]. The microstructures of SLM AlSi10Mg were observed with an optical microscope and a scanning electron microscope (SEM). Due to material anisotropy, two sections (i.e. section along the build orientation and section perpendicular to the build orientation) of both 0° built and 90° built specimens were observed. The microstructures of two specimens by optical microscopy are shown in Fig. 6.

From Fig. 6, it is seen that there is no obvious difference in the microstructures between 0° built specimen (as shown in Fig. 6a and b) and 90° built specimen (as shown in Fig. 6c and d). For both 0° built and 90° built specimens, the section along the build orientation shows a

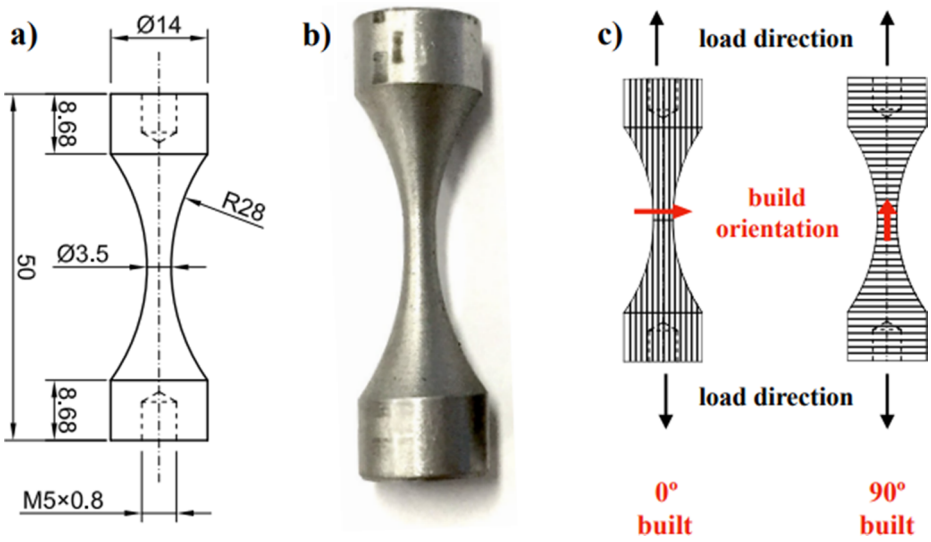

Fig. 2. Hourglass specimen used in fatigue tests: a) specimen geometry (dimensions in mm), b) specimen photo and c) schematic of build orientation.

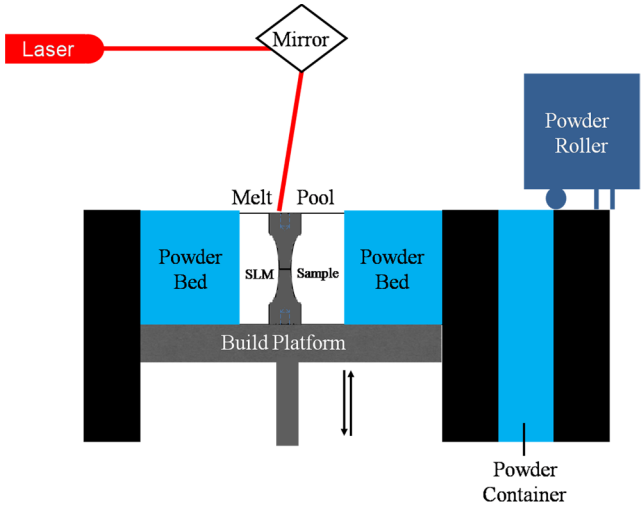

Fig. 3. Schematic of SLM process.

fish-scale pattern, which is formed during the SLM process [43,44]. The fish-scale pattern consists of semi-elliptical melt pool, which is a characteristic of SLM technology. The segments in Fig. 6b and 6c are not continuous because the laser beam may penetrate the previous layer when melting. In addition, hatch distance measured from Fig. 6b and c is about 200 μm, which is very close to the set value 190 μm. As a consequence, it is the laser process parameters rather than the build orientation that determines the microstructure of the material. As the section along build orientation is made up of melt zone, it is important to investigate the structure of melt zone, which is caused by the Gaussian distribution of laser power. The powders scanned by middle portion of a laser beam absorbed more energy than that scanned by its edge portion. As a result, some powders completely melted and others not, which resulted in the melt pool structure. From inner to outer, melt pool is divided into three zones, i.e. the fine zone, coarser zone and heat affected zone (HAZ). The temperature decreases from inner zone to outer zone, which resulted in the formation of different microstructures in the three zones.

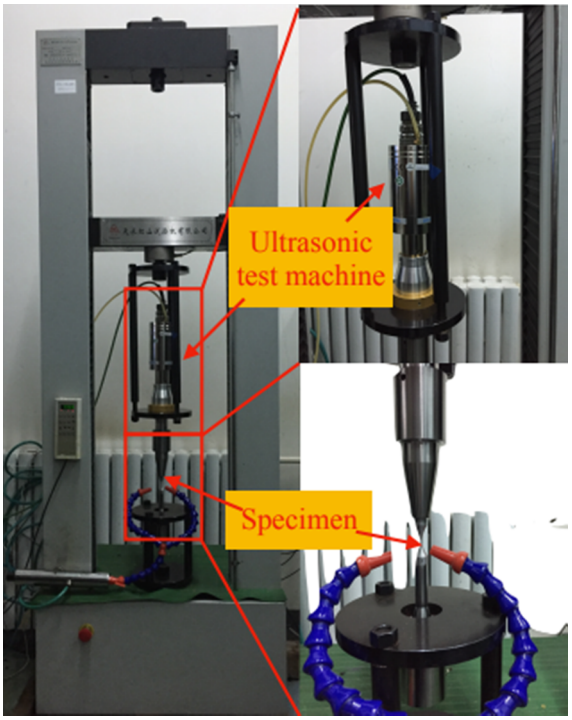

Fig. 4. Ultrasonic fatigue testing machine: ultrasonic device connected with a tensile machine.

More microstructure information was observed with SEM, as presented in Fig. 7. Both the melt pool boundary (MPB) and the HAZ can be clearly seen in Fig. 7a. A coarse zone is located at the MPB and it consists of relatively coarse microstructures. At higher magnification (Fig. 7d), it is clear that the coarse zone contains numerous small pores, which were formed due to shrinkage during solidification, as explained

Table 2
SLM manufacturing parameters of AlSi10Mg specimen.

Laser power [W]	Scanning speed [mm/s]	Scanning spacing [mm]	Preheating temperature [°C]	Powder size [mm]	Printing direction [°]	Laser beam profile
370	1300	0.19	35	0.05	0, 90	Gaussian

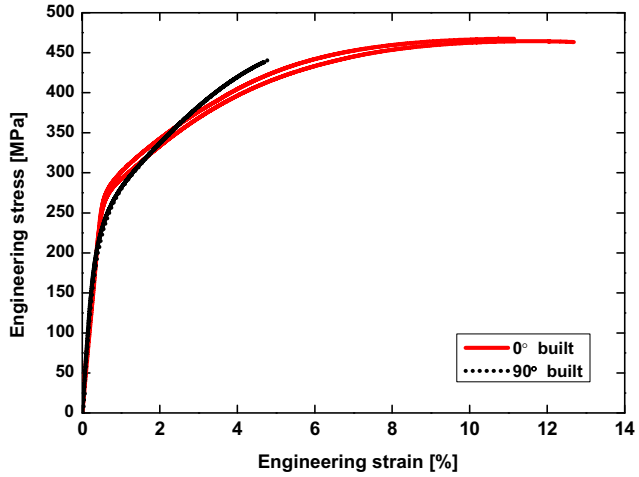

Fig. 5. Results of tensile tests for AlSi10Mg specimens with two build orientations.

by [35]. The fine cellular structure composed of α-Al and eutectic Si (Fig. 7b) can be seen from the section along the build orientation. It is generally accepted that the fine eutectic Si helps improve mechanical properties of the material. The section perpendicular to the build orientation has elongated structure instead of equiaxed structure.

3.3. S-N data

The S-N data for both 0° built and 90° built specimens are plotted in Fig. 8a. According to the Basquin relation $\Delta\sigma \cdot N^{-a} = C$, the S-N data can be approximately fitted by the curves shown in Fig. 8a. It is indicated that tensile mean stress plays an important role in HCF and VHCF property of the specimens. With the increase of mean stress, the fatigue strength decreases, which agrees with [45,46]. In addition, the build orientation has an important effect on the fatigue property. As shown in Fig. 8a, the fatigue strength of 90° built specimens is obviously lower than that of 0° built specimens. One reason is that different stresses act on the specimens manufactured at different orientations. The other reason may be due to the fact that the defect size of 90° built specimens is larger than that of 0° built specimens, as reported in [46]. The variation of fatigue strength with build orientation is also in agreement with that of tensile strength, as described in Section 3.1.

A probabilistic model proposed in [47] was applied to perform a P-S-N study from a statistical point of view. The conditional fatigue life is assumed to be a normal random variable with mean μ_Y and standard deviation σ_Y. The standard deviation is constant and the mean can be expressed with logarithm of stress amplitude × and logarithm of initial defect size, $\log_{10}(\sqrt{a_{d,0}})$ as follows:

$$\sigma_Y = c_Y + m_Y x + n_Y \log(\sqrt{a_{d,0}}) \tag{1}$$

where c_Y, m_Y, n_Y are constants estimated from experimental data and $\sqrt{a_{d,o}}$ is initial defect size, measured by the methods described in [47]. According to the statement that one failure mode is due to one cause with fatigue limit described in [47],

$$F_Y = (y; x, \sqrt{a_{d,0}}) = F_{X_l}(x, \sqrt{a_{d,0}}) F_{Y_f}(y) \tag{2}$$

By combining quantile definition, the relationship between fatigue life and stress can be expressed as:

$$y = \mu_Y(x, \sqrt{a_{d,0}}) + \sigma_Y \Phi^{-1}_{Gauss}\left[\frac{\alpha}{\Phi_{Gauss}}\left(\frac{x - \mu_{X_l}(\sqrt{a_{d,0}})}{\sigma_{X_l}}\right)\right] \tag{3}$$

With this model, the conditional P-S-N curves related to initial defect size are obtained in Fig. 8b. According to Fig. 8b, the probabilistic model is in good agreement with experiments, i.e. a confidence interval of 90% covers most of experimental data. Therefore, it is practical to apply this approach as design curve in engineering applications.

3.4. Fractography

The fracture surfaces of failed specimens were observed by SEM in order to obtain more information on the crack initiation. The fracture surface can be roughly divided into three zones according to their

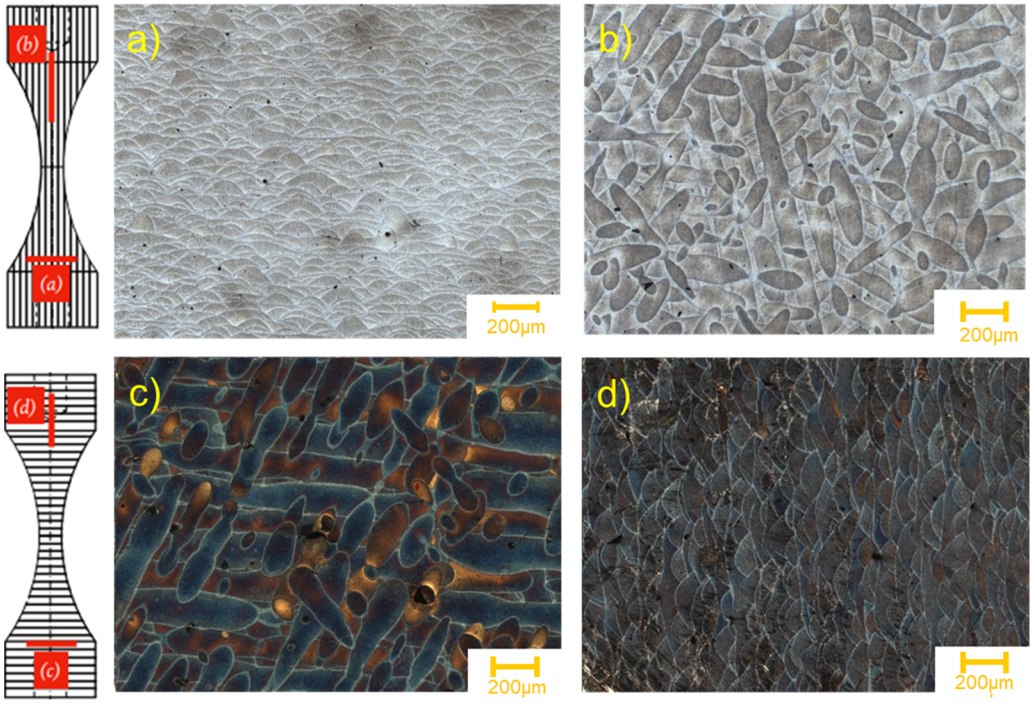

Fig.6. Microstructure of 0° and 90° built specimens: a) section along build orientation, b) section perpendicular to build orientation for 0°built specimen, c) section perpendicular to build orientation for 90° built specimen and d) section along build orientation for 90° built specimen.

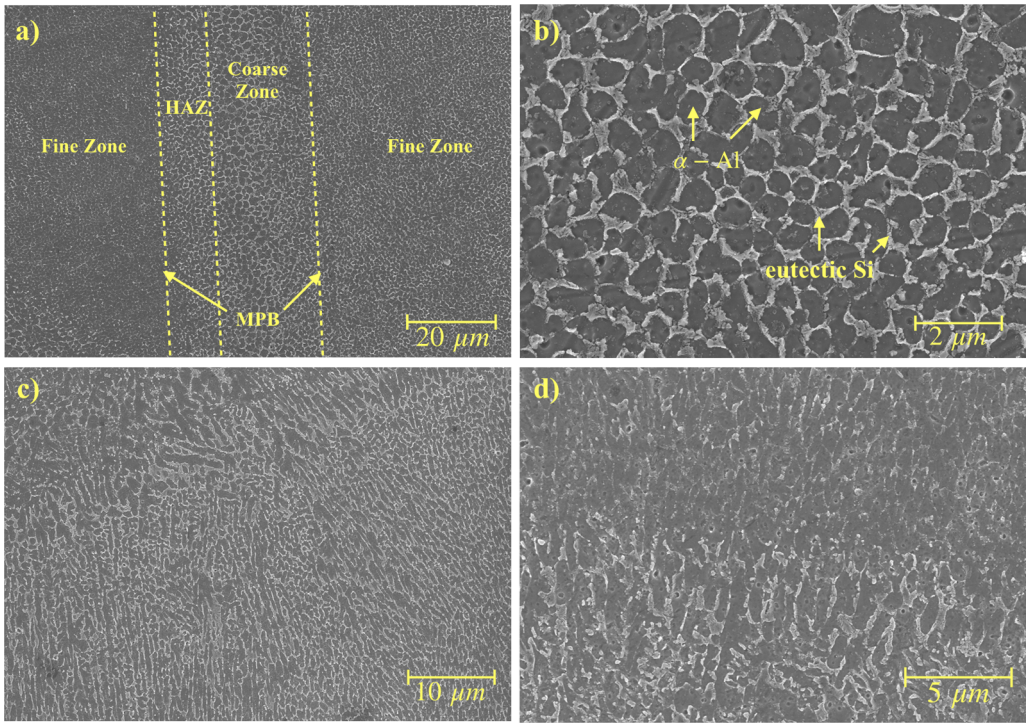

Fig. 7. SEM images of SLM AlSi10Mg: a) section along build orientation, b) equiaxed cellular structure, c) section perpendicular to build orientation, and d) coarse zone.

features under SEM, as shown in Fig. 9a and b. A smooth zone in SEM image is formed by crack initiation and slow propagation, which is called initiation zone. In general, initiation zone includes an initial defect where crack initiates and a zone caused by crack slow propagation. In the case of surface initiation, initiation zone tends to be a semi-circle. In contrast, it is a circle if crack initiates from interior. This usually happens in VHCF regime for both conventionally fabricated materials [48-50] and AM materials [51,52]. Initiation zone contains a fisheye pattern in this case.

For specimens with different build orientations, sizes of fisheye vary greatly. Fig. 9c and d present fisheye in 0° built specimen and in 90° built specimen, respectively. The size of fisheye in 90° built specimen is usually much larger than that in 0° built specimen, due to the difference in the melt pool structure. For 0° built specimen, the crack propagates across build layers, i.e., crack needs to cross the melt pool, as shown in Fig. 9c. Fine particle area (FPA), where the microstructure is very fine, takes up most area of the melt pool. Consequently, a crack is most possible to initiate in the melt zone. The temperature near the center of melt pool is high and the structure is fine relatively. Therefore the crack is difficult to propagate in FPA. Hence, the initiation zone is small in this case. However, for 90° built specimen, crack propagates almost in the same layer, as shown in Fig. 9d. The existence of discontinuity helps crack propagation, such that the initiation size is relatively large.

The crack initiation mechanism was further studied and four crack

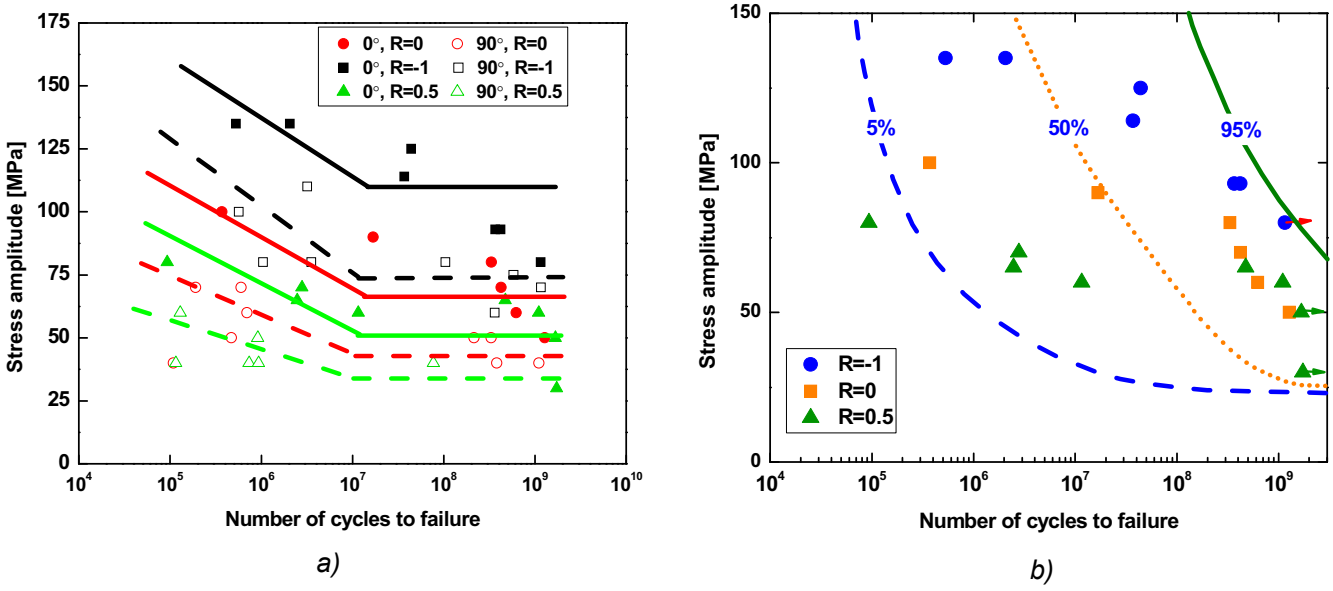

Fig. 8. a) S-N data for specimens made with different orientations and under different mean stresses, b) conditional P-S-N curves.

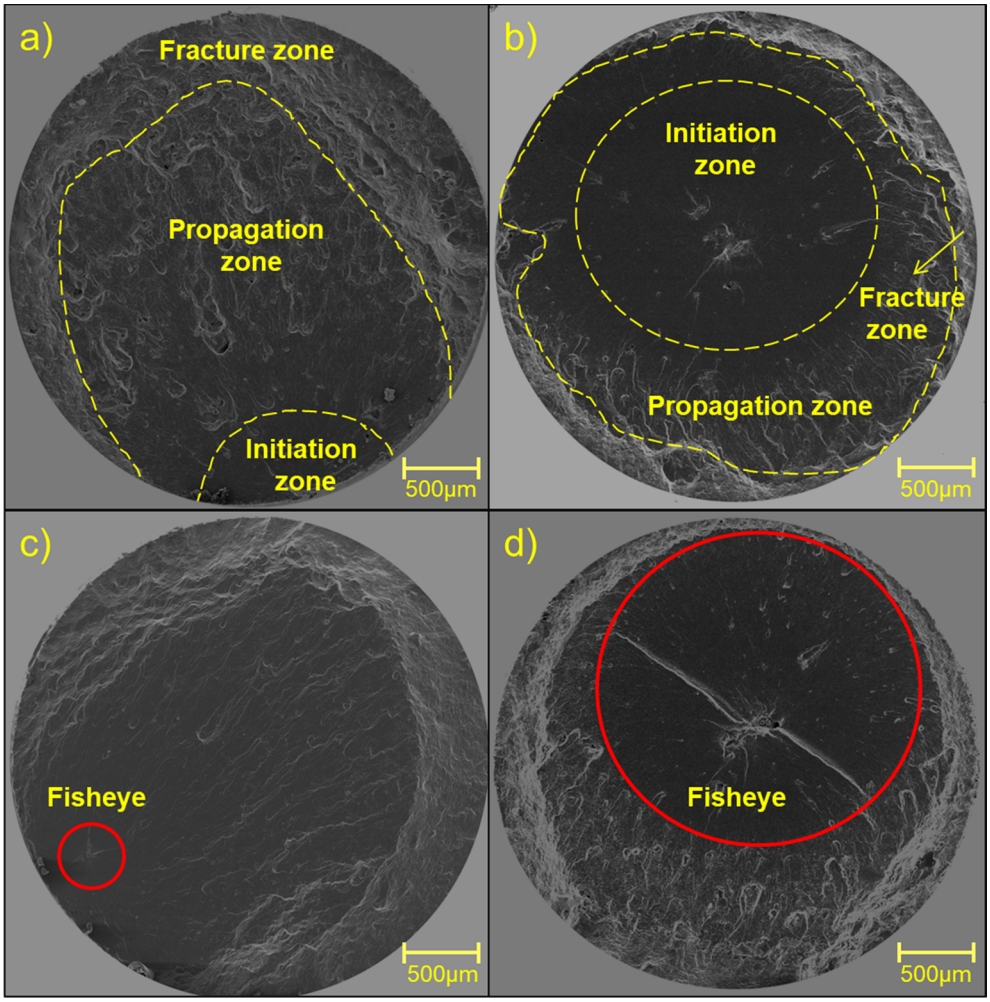

Fig. 9. Fracture surface of 0° built and 90° built specimens: a) crack initiated from surface, the initiation zone is usually a semi-circle. b) crack initiated from interior, the initiation zone is usually a circle, forming a fisheye pattern. c) fracture surface of 0° built specimen. d) fracture surface and fisheye pattern in 90° built specimen. Fisheye is marked by red circle.

initiation patterns were identified, namely initiation by lack-of-fusion (inclusion), initiation by internal pore, initiation with no obvious defect and initiation by tearing, as shown in Fig. 10a-d. The most common pattern of failure in the specimens is lack-of-fusion (Fig. 10a). This type of failure initiated from all three locations, i.e. surface, subsurface and interior. Fatigue failure by internal pore is shown in Fig. 10b. It is reasonable that SLM specimen has some pores of small size. However, the well-set SLM processing parameters ensure that most of the pore sizes are below the threshold to initiate a crack. The only exception case that initiated from internal pore occurred in VHCF regime. In addition, it is interesting that failure could happen with no obvious appearance of defect, as shown in Fig. 10c. This type of failure could be explained by stress concentration effect. The stress concentration at rough surface has an important influence on crack initiation under high stress. The last failure type is by tearing in VHCF regime, as shown in Fig. 10d. It is clear that a layer of material is torn and internal material is thus exposed. The exposed internal material looks very smooth and the melt pool is clearly seen in Fig. 10e. The melt pool is fragile and the microstructure is discontinuous. Therefore, a part of material is torn out and crack initiated under cyclic stress.

3.5. Fracture mechanics parameter

Stress intensity factor (SIF) plays an important role in fatigue failure. According to Murakami [53], SIF is calculated by:

$$\Delta K = Y \Delta\sigma \sqrt{\pi a} \tag{4}$$

where $Y = 0.5$ for internal crack initiation and $Y = 0.65$ for surface crack initiation. The crack depth parameter a is estimated directly by measuring the initiation defect size from the fracture surface. The equivalent semi-length of crack is calculated by:

$$a = \sqrt{area/\pi} \tag{5}$$

By substituting Eq. (5) into Eq. (4), the threshold of fatigue crack growth is:

$$\Delta K_{th} = Y \Delta\sigma \sqrt{\sqrt{\pi \cdot area}} \tag{6}$$

The calculated ΔK_{th} is around 1.5 MPa$\sqrt{m}$, which is very close to that in [54-56], as shown in Fig. 11a. In addition, tensile mean stress has no obvious effect on this threshold, which is due to the fact that ΔK_{th} is the boundary for propagation while mean stress has an influence on the propagation rate.

The threshold for crack stable propagation zone denoted as ΔK_p is further calculated with Eq. (6), as shown in Fig. 11b. It is shown that with increasing tensile mean stress (from $R = -1$ to $R = 0.5$), ΔK_p decreases. The interesting fact is that for the same R, the propagation threshold increases with the initiation zone. According to Eq. (4), ΔK_p is determined by the applied stress and the area of initiation zone and ΔK_p increases with area of initiation zone. This implies that it is the tensile mean stress that dominates crack initiation and early slow propagation.

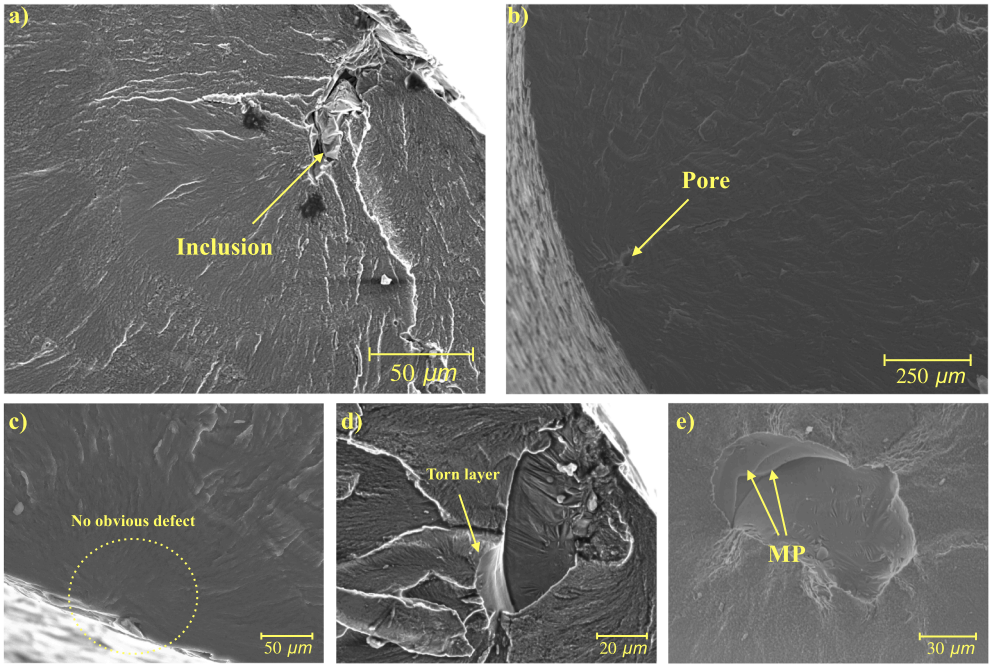

Fig. 10. Four patterns of crack initiation: a) initiation by inclusion (lack-of-fusion), b) initiation by internal pore, c) initiation with no obvious defect, d) initiation by tearing, e) initiation by tearing with melt pool (MP).

3.6. Modified Murakami model

According to the Murakami model [50,53], fatigue strength σ_w in HCF and VHCF regimes is predicted by

$$\sigma_\omega = C\frac{(HV+120)}{(\sqrt{area})^{1/6}}\left(\frac{1-R}{2}\right)^{\alpha} \tag{7}$$

where C takes 1.43 (or 1.56) for surface (or internal) crack initiation and $\alpha = 0.226 + HV \times 10^{-4}$. The difference between surface and internal crack initiation is due to the distance from initiation defect to fracture surface. The model has been applied for many materials [57–59]. In an attempt to use the model for both surface and internal crack initiation, new variable distance and r were defined in Fig. 12a.

Considering that the coefficient of internal (or surface) crack initiation and hardness of material are both constant, a new combined material constant C_m was defined. Furthermore, the distance variable may not be adequacy to represent the fatigue failure as the specimen geometry could also have an effect on the crack initiation. The radius of fracture surface r was thus introduced and the ratio of distance to r was used. Therefore, a modified model to include crack initiation effect is written by:

$$\sigma_\omega = C_m f\left(\sqrt{area}, R, \frac{distance}{r}\right) \tag{8}$$

With inspiration from Murakami's model, the new model is expressed:

$$\sigma = \frac{C_m}{\sqrt{area}^{\beta_1}}\left(\frac{1-R}{2}\right)^{\beta_2}\exp\left(\beta_3\sqrt{1-\frac{distance}{r}}\right) \tag{9}$$

or in logarithm form:

$$\log\sigma_w = \log C_m - \beta_1\log\sqrt{area} + \beta_2\log\left(\frac{1-R}{2}\right) + \beta_3\sqrt{1-\frac{distance}{r}} \tag{10}$$

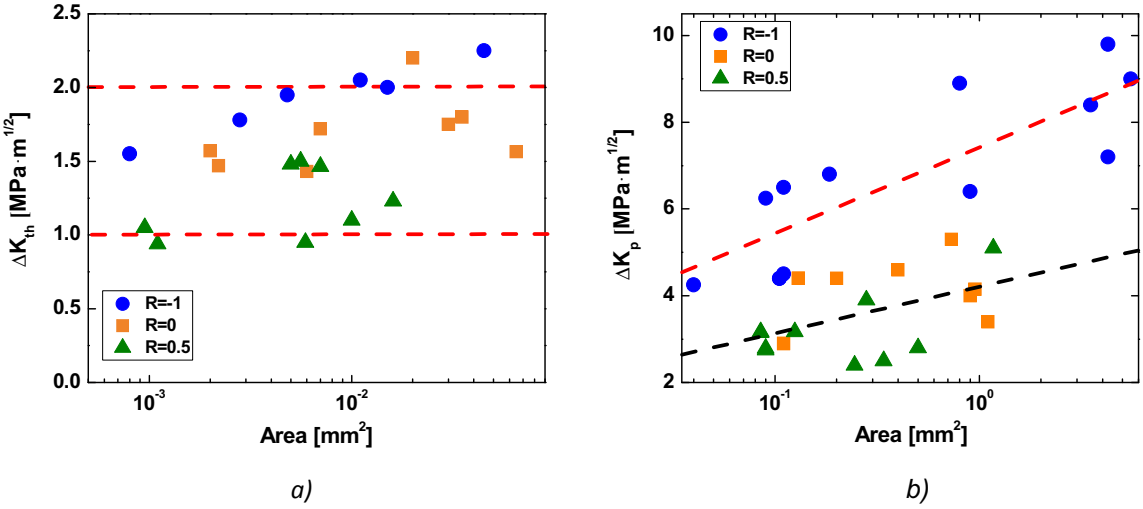

Fig. 11. a) Fatigue crack propagation threshold, b) Threshold for crack stable propagation. The tensile mean stress does have an influence on crack propagation rate.

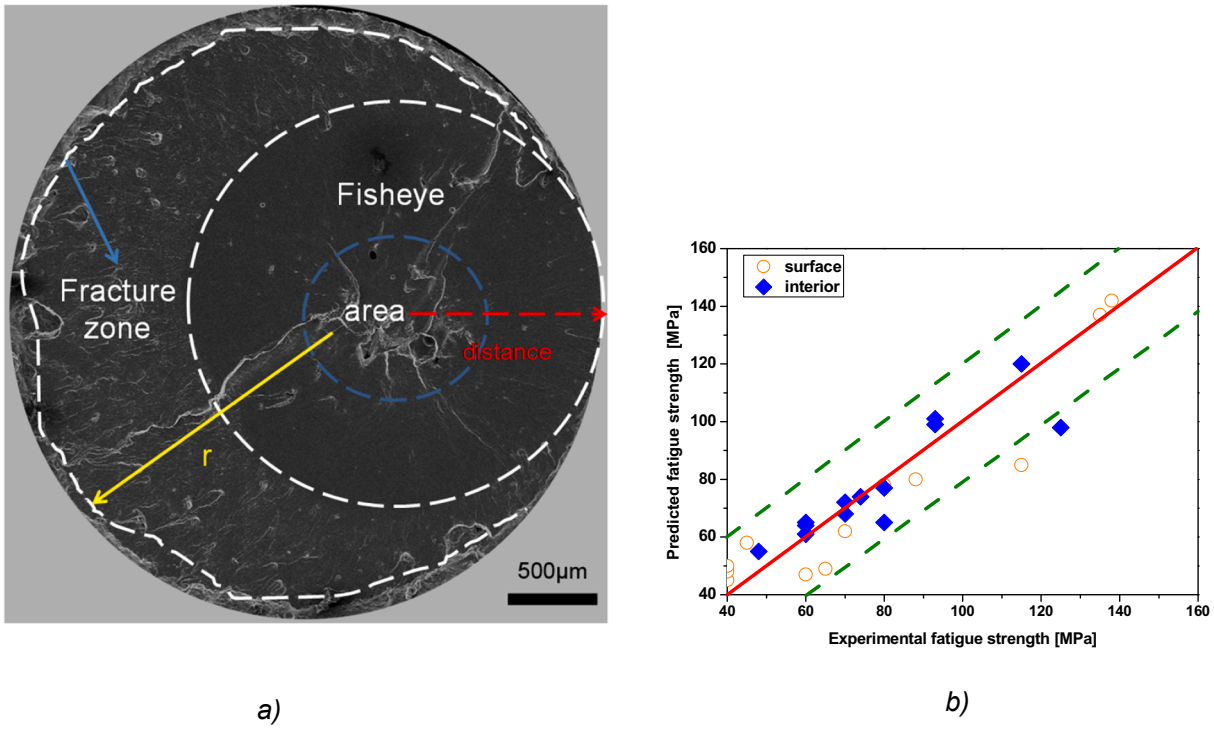

Fig. 12. a) A modified Murakami model: schematic of new distance used to unify fatigue strength. ($R = -1$, $\sigma_a = 60$ MPa, $N = 3.63\text{x}10^8$), b) Comparison of predicted fatigue strength σ_a with experimental results.

where C_m, β_1, β_2, β_3 are constants that can be determined by linear regression using the least square method. The comparison of the model prediction with the experimental results is shown in Fig. 12b. It is seen that the proposed model well predicts the fatigue strength for both internal and surface crack initiation.

4. Conclusions

This paper investigated the influence of build orientation and mean stress on the HCF and VHCF property of AlSi10Mg alloy fabricated by SLM. The main conclusions are as follows:

(1) The build orientation has great effect on mechanical properties and fatigue performance of SLM AlSi10Mg. Horizontally built specimen has better performance than vertically built specimen, especially in tensile strength, elongation and fatigue property.
(2) Four crack initiation modes are identified for SLM AlSi10Mg in HCF and VHCF regimes, namely initiation by lack-of-fusion, by internal pore, with no obvious defect and by tearing. Fisheye patter with different morphology is observed in VHCF for the specimens manufactured with different orientations.
(3) The crack propagation threshold for AlSi10Mg is about 1.5 MPa$\sqrt{\text{m}}$. Tensile mean stress reduces the fatigue life by reducing the life for crack initiation and early growth.
(4) A model proposed in this paper well describes the effect of crack initiation on fatigue strength of SLM AlSi10Mg.

Acknowledgements

This work was supported by the NSFC Basic Science Center Program for “Multiscale Problems in Nonlinear Mechanics” (No. 11988102), by the National Natural Science Foundation of China (No. 11932020, 11872364, 11902370), CAS Pioneer Hundred Talents Program, Guangdong Major Project of Basic and Applied Basic Research (2019B030302011), Guangdong Basic and Applied Basic Research Foundation (2019A050510022), Key-Area R&D Program of GuangDong Province (2019B010943001).

References

[1] Wong K, Hernandez A. A review of additive manufacturing. ISRN Mech Eng 2012.
[2] Li X, Ji G, Chen Z, Addad A, Wu Y, Wang H, et al. Selective laser melting of nano-TiB2 decorated AlSi10Mg alloy with high fracture strength and ductility. Acta Mater 2017;129:183–93.
[3] Suryawanshi J, Prashanth K, Scudino S, Eckert J, Prakash O, Ramamurty U. Simultaneous enhancements of strength and toughness in an Al12Si alloy synthesized using selective laser melting. Acta Mater 2016;115:285–94.
[4] Martin J, Yahata B, Hundley J, Mayer J, Schaedler T, Pollock T. 3D printing of high-strength aluminium alloys. Nature 2017;549:365–9.
[5] Pauly S, Löber L, Petters R, Stoica M, Scudino S, Kühn U, et al. Processing metallic glasses by selective laser melting. Mater Today 2013;16(1):37–41.
[6] Li X, Roberts M, Liu Y, Kang C, Huang H, Sercombe T. Effect of substrate temperature on the interface bond between support and substrate during selective laser melting of Al–Ni–Y–Co–La metallic glass. Mater Des 2015;65:1–6.
[7] Li X, Kang C, Huang H, Zhang L, Sercombe T. Selective laser melting of an Al86Ni6Y4.5Co2La1.5 metallic glass: Processing, microstructure evolution and mechanical properties. Mater Sci Eng A 2014;606:370–9.
[8] Khanzadeh M, Tian W, Yadollahi A, Doude H, Tschopp M, Bian L. Dual process monitoring of metalbased additive manufacturing using tensor decomposition of thermal image streams. Addi Manu 2018;23:443–56.
[9] Wohlers T, Associates W, Campbell R, Caffrey T. Wohlers Report 2016: 3D Printing and Additive Manufacturing State of the Industry: Annual Worldwide Progress Report. Wohlers Associates, 2016.
[10] Khairallah S, Anderson A, Rubenchik A, King W. Laser powder-bed fusion additive manufacturing: Physics of complex melt flow and formation mechanisms of pores, spatter, and denudation zones. Acta Mater 2016;108:36–45.
[11] Read N, Wang W, Essa K, Attallah M. Selective laser melting of AlSi10Mg alloy: process optimisation and mechanical properties development. Mater Des 2015;65:417–24.
[12] Tridello A, Biffi CA, Fiocchi J, Bassani P, Chiandussi G, Rossetto M, et al. VHCF response of as-built SLM AlSi10Mg specimens with large loaded volume. Fatigue Fract Eng Mater Struct 2018;41:1918–28.
[13] Pan X, Su H, Sun C, Hong Y. The behavior of crack initiation and early growth in high-cycle and very-high-cycle fatigue regimes for a titanium alloy. Int J Fatigue 2018;115:67–78.
[14] Qian G, Zhou C, Hong Y. Experimental and theoretical investigation of environmental media on very-high-cycle fatigue behavior for a structural steel. Acta Mater 2011;59:1321–7.
[15] Tradowsky U, White J, Ward R, Read N, Reimers W, Attallah M. Selective laser melting of AlSi10Mg: Influence of post-processing on the microstructural and tensile properties development. Mater Des 2016;105:212–22.
[16] Günther J, Krewerth D, Lippmann T, Leuders S, Tröster T, Weidner A, et al. Fatigue

life of additively manufactured Ti–6Al–4V in the very high cycle fatigue regime. Int J Fatigue 2017;94:236–45.
[17] Razavi SMJ, Berto F. Directed energy deposition versus wrought Ti-6Al-4V: a comparison of microstructure, fatigue behavior, and notch sensitivity. Adv Eng Mater 2019;21(8):1900220.
[18] Yates JR, Efthymiadis P, Antonysamy AA, Pinna C, Tong J. Do additive manufactured parts deserve better? Fatigue Fract Eng Mater Struct 2019;42:2146–54.
[19] Qian G, Jian Z, Pan X, Berto F. In-situ investigation on fatigue behaviors of Ti-6Al-4V manufactured by selective laser melting. Int J Fatigue 2020;133:105424.
[20] Qian G, Li Y, Tridello A, Paolino D, Berto F, Hong Y. Very-high-cycle fatigue behavior of Ti-6Al-4V manufactured by selective laser melting: Effect of build orientation. Int J Fatigue 2020;136:105628.
[21] Hu Y, Wu S, Wu Z, Zhong X, Ahmed S, Karabal S, et al. A new approach to correlate the defect population with the fatigue life of selective laser melted Ti-6Al-4V. Int J Fatigue 2020;136:105584.
[22] Liu B, Wang K, Bao R, Sui F. The effects of α/β phase interfaces on fatigue crack deflections in additively manufactured titanium alloy: a peridynamic study. Int J Fatigue 2020:105631.
[23] Xu S, Zhu S, Hao Y, Qian G. A new critical plane-energy model for multiaxial fatigue life prediction of turbine disc alloys. Eng Fail Anal 2018;93:55–63.
[24] Liu X, Chen E, Zeng F, Cong T, Domblesky J. Mechanisms of interior crack initiation in very-high-cycle fatigue of high-strength alloys. Eng Fract Mech 2019;212:153–63.
[25] Qian G, Lei W. A statistical model of fatigue failure incorporating effects of specimen size and load amplitude on fatigue life. Philos Mag 2019;99:2089–125.
[26] Liao D, Zhu S, Qian G. Multiaxial fatigue analysis of notched components using combined critical plane and critical distance approach. Int J Mech Sci 2019;160:38–50.
[27] Cong T, Han J, Hong Y, Domblesky J, Liu X. Shattered rim and shelling of high-speed railway wheels in the very-high-cycle fatigue regime under rolling contact loading. Eng Fail Anal 2019;97:556–67.
[28] Hu D, Wang T, Ma Q, Liu X, Shang L, Li D, et al. Effect of inclusions on low cycle fatigue lifetime in a powder metallurgy nickel-based superalloy FGH96. Int J Fatigue 2019;118:237–48.
[29] Kahlin M, Ansell H, Moverare JJ. Fatigue behaviour of notched additive manufactured Ti6Al4V with as-built surfaces. Int. J. Fatigue 2017;101:51.
[30] Liu X, Wang R, Hu D, Mao J. A calibrated weakest-link model for probabilistic assessment of LCF life considering notch size effects. Int J Fatigue 2020;105631.
[31] Hu Y, Wu S, Withers P, Zhang J, Bao H, Fu Y, et al. The effect of manufacturing defects on the fatigue life of selective laser melted Ti-6Al-4V structures. Mater Des 2020;192:108708.
[32] Zhao J, Easton M, Qian M, Leary M, Brandt M. Effect of building direction on porosity and fatigue life of selective laser melted AlSi12Mg alloy. Mater Sci Eng A 2018;729:76–85.
[33] Walker K, Liu Q, Brandt M. Evaluation of fatigue crack propagation behaviour in Ti-6Al-4V manufactured by selective laser melting. Int J Fatigue 2017;104:302–8.
[34] Tridello A, Fiocchi J, Biffi CA, Chiandussi G, Rossetto M, Tuissi A, et al. Influence of the annealing and defects on the VHCF behavior of an SLM AlSi10Mg alloy. Fatigue Fract Eng Mater Struct 2019;42:2794–807.
[35] Aboulkhair N, Maskery I, Tuck C, Ashcroft I, Everitt N. Improving the fatigue behaviour of a selectively laser melted aluminium alloy: Influence of heat treatment and surface quality. Mater Des 2016;104:174–82.
[36] Srinivas M, Sridhar Babu B. A Critical Review on Recent Research Methodologies in Additive Manufacturing. Materials Today: Proceedings, 4(8):9049 – 9059, 2017. International Conference on Advancements in Aeromechanical Materials for Manufacturing (ICAAMM-2016): Organized by MLR Institute of Technology, Hyderabad, Telangana, India.
[37] Benedetti M, Fontanari V, Bandini M, Zanini F, Carmignato S. Low- and high-cycle fatigue resistance of Ti-6Al-4V ELI additively manufactured via selective laser melting: Mean stress and defect sensitivity. Int J Fatigue 2018;107:96–109.
[38] Wang Z, Wu W, Qian G, Correia J, Sun L. In-situ SEM investigation on fatigue behaviors of additive manufactured Al-Si10-Mg alloy at elevated temperature. Eng Fract Mech 2019;214:149–63.
[39] Xiong Z, Liu S, Li S, Shi Y, Yang Y, Misra R. Role of melt pool boundary condition in determining the mechanical properties of selective laser melting AlSi10Mg alloy. Mater Sci Eng A 2019;740–741:148–56.
[40] Agius D, Kourousis K, Wallbrink C, Song T. Cyclic plasticity and microstructure of as-built SLM Ti-6Al-4V: the effect of build orientation. Mater Sci Eng A 2017;701:85–100.
[41] Thijs L, Kempen K, Kruth J, Van Humbeeck J. Fine-structured aluminium products with controllable texture by selective laser melting of pre-alloyed AlSi10Mg powder. Acta Mater 2013;61:1809–19.
[42] Tomus D, Tian Y, Rometsch P, Heilmaier M, Wu X. Influence of post heat treatments on anisotropy of mechanical behaviour and microstructure of hastelloy-x parts produced by selective laser melting. Mater Sci Eng A 2016;667:42–53.
[43] Zhou L, Mehta A, Schulz E, McWilliams B, Cho K, Sohn Y. Microstructure, precipitates and hardness of selectively laser melted AlSi10Mg alloy before and after heat treatment. Mater Charact 2018;143:5–17.
[44] Rosenthal I, Stern A, Frage N. Strain rate sensitivity and fracture mechanism of AlSi10Mg parts produced by Selective Laser Melting. Mater Sci Eng A 2017;682:509–17.
[45] Sarkar S, Siva Kumar C, Nath A. Effect of mean stresses on mode of failures and fatigue life of selective laser melted stainless steel. Mater Sci Eng A 2017;700:92–106.
[46] Larrosa N, Wang W, Read N, Loretto M, Evans C, Carr J, et al. Linking microstructure and processing defects to mechanical properties of selectively laser melted AlSi10Mg alloy. Theo Appl Fract Mech 2018;98:123–33.
[47] Paolino D, Tridello A, Chiandussi G, Rossetto M. S-N curves in the very-high-cycle fatigue regime: statistical modeling based on the hydrogen embrittlement consideration. Fatigue Fract Eng Mater Struct 2016;39:1319–36.
[48] Naito T, Ueda H, Kikuchi M. Fatigue behavior of carburized steel with internal oxides and nonmartensitic microstructure near the surface. Met Trans A 1984;15:1431–6.
[49] Milošević I, Renhart P, Winter G, Grün F, Kober M. Validation of a new high frequency testing technique in the VHCF regime – Fatigue properties of a 42CrMoS4 and X5CrNiCuNb16-4 steel. Int J Fatigue 2018;112:198–205.
[50] Jeddi D, Palin-Luc T. A review about the effects of structural and operational factors on the gigacycle fatigue of steels. Fatigue Fract Eng Mater Struct 2018;41:969–90.
[51] Romano S, Patriarca L, Foletti S, Beretta S. LCF behaviour and a comprehensive life prediction model for AlSi10Mg obtained by SLM. Int J Fatigue 2018;117:47–62.
[52] Cao F, Ravi Chandran K. The role of crack origin size and early stage crack growth on high cycle fatigue of powder metallurgy Ti-6Al-4V alloy. Int J Fatigue 2017;102:48–58.
[53] Murakami Y. Chapter 2 - stress concentration. In Yukitaka Murakami, editor, Metal Fatigue, pages 11 – 24. Elsevier Science Ltd, Oxford, 2002.
[54] Tridello A, Paolino D, Chiandussi G, Rossetto M. VHCF Response of H13 Steels Produced with Different Manufacturing Processes. Procedia Engineering, 160:93 – 100, 2016. XVIII International Colloquium on Mechanical Fatigue of Metals (ICMFM XVIII), Gijón (Spain), September 5-7, 2016.
[55] Romano S, Brückner-Foit A, Brandão A, Gumpinger J, Ghidini T, Beretta S. Fatigue properties of AlSi10Mg obtained by additive manufacturing: defect-based modelling and prediction of fatigue strength. Eng Fract Mech 2018;187:165–89.
[56] Shojima K, Weldle S, Okazaki S, Endo M, Eifler D, Balle F. Notch effects in high cycle fatigue of Ti-6Al-4V. Advanced Materials Science and Technology, volume 750 of Materials. Science Forum, vol. 5. Trans Tech Publications; 2013. p. 232–5.
[57] Masuo H, Tanaka Y, Morokoshi S, Yagura H, Uchida T, Yamamoto Y, et al. Influence of defects, surface roughness and HIP on the fatigue strength of Ti-6Al-4V manufactured by additive manufacturing. Int J Fatigue 2018;117:163–79.
[58] Åman M, Tanaka Y, Murakami Y, Remes H, Marquis G. Fatigue strength evaluation of small defect at stress concentration. Proc Struct Int 2017;7:351–8.
[59] Furuya Y. A new model for predicting the gigacycle fatigue strength of high-strength steels. Mater Sci Eng A 2019;743:445–52.